Reduced-order prediction of rogue waves in two-dimensional deep-water waves

CrossMark

Mohammad Farazmand, Themistoklis P. Sapsis *

Department of Mechanical Engineering, Massachusetts Institute of Technology, 77 Massachusetts Ave., Cambridge, MA 02139, United States

A B S T R A C T

We consider the problem of large wave prediction in two-dimensional water waves. Such waves form due to the synergistic effect of dispersive mixing of smaller wave groups and the action of localized nonlinear wave interactions that leads to focusing. Instead of a direct simulation approach, we rely on the decomposition of the wave field into a discrete set of localized wave groups with optimal length scales and amplitudes. Due to the short-term character of the prediction, these wave groups do not interact and therefore their dynamics can be characterized individually. Using direct numerical simulations of the governing envelope equations we precompute the expected maximum elevation for each of those wave groups. The combination of the wave field decomposition algorithm, which provides information about the statistics of the system, and the precomputed map for the expected wave group elevation, which encodes dynamical information, allows (i) for understanding of how the probability of occurrence of rogue waves changes as the spectrum parameters vary, (ii) the computation of a critical length scale characterizing wave groups with high probability of evolving to rogue waves, and (iii) the formulation of a robust and parsimonious reduced-order prediction scheme for large waves. We assess the validity of this scheme in several cases of ocean wave spectra.

© 2017 Elsevier Inc. All rights reserved.

1. Introduction

Rogue waves refer to extremely large oceanic surface waves. As a result of their devastating impact on marine systems, such as ships and offshore platforms, rogue waves have been the subject of numerous theoretical, experimental and numerical studies [6,14,32]. Most studies concern the frequency and statistics of rogue wave occurrence for a given sea state (see, e.g., [20,25,26,40,47]). It is, however, often desirable to know, for a given ocean area, *if*, *when* and *where* a rogue wave may occur in the future.

These questions can in principle be addressed by numerically solving the appropriate hydrodynamic equations [7,13,27]. Apart from its high computational cost, this direct approach requires a well-resolved state of the fluid velocity field and its free surface elevation as initial conditions. Thanks to recent developments, real-time and reliable measurement of sea surface elevation is feasible (see e.g. [22,28,29,39,41]). But the well-resolved measurement of fluid velocity field remains out of reach.

An alternative approach for short-term prediction of the wave field is based on numerically solving the so-called envelope equations, which approximate the evolution of the wave envelope to a reasonable accuracy [15,42,48]. While less

---

* Corresponding author.
  E-mail addresses: mfaraz@mit.edu (M. Farazmand), sapsis@mit.edu (T.P. Sapsis).
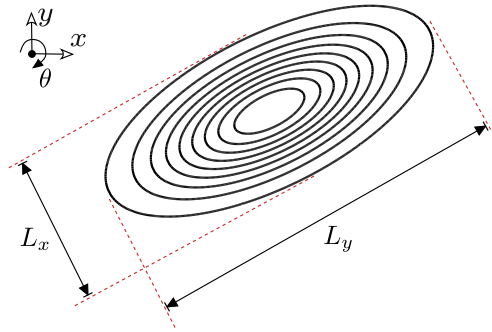
Fig. 1. Schematic view of an elementary wave group (EWG) with a Gaussian profile.

expensive than the full hydrodynamic equations, solving the envelope equations is still computationally formidable for real-time forecast of extreme waves.

As a result, several attempts have been made to devise reliable, reduced-order methods for short-time forecast of water wave evolution. Adcock et al. [1], for instance, approximate nonlinear evolution of localized wave groups with an exact breather-like solution of the linear Schrödinger equation. To account for the nonlinear effects, they allow the parameters of the breather-like solution to vary in time such that particular invariants (energy and the Hamiltonian) of the nonlinear Schrödinger equation (NLS) are preserved over time. Ruban [36] takes a similar approach by substituting a Gaussian ansatz into the Lagrangian functional associated with the NLS equation. The time evolution of the parameters are determined such that the solution satisfies a least-action principle (also see [35]).

The resulting wave groups from Adcock et al. [1] and Ruban [35] do not necessarily satisfy the underlying envelope equation (i.e., the NLS equation). Furthermore, the reduced-order method of Ruban [35] relies heavily on the Lagrangian formulation of the NLS equation. As such, it is not immediately applicable to the more realistic, higher-order envelope equations, such as the modified NLS (MNLS) equation of Dysthe [15], whose Lagrangian formulation is unavailable (see [23] and [12] for the Hamiltonian formulation of the MNLS equation).

To avoid these drawbacks, Cousins and Sapsis [8,10] take an intermediate approach. They also consider the evolution of parametric wave groups but allow the wave group to evolve under the full nonlinear evolution equation by imposing energy conservation [9]. The analysis resulted in a reduced-order set of nonlinear equations that captures the nonlinear dynamics of wave groups and most critically their transition from defocussing to focusing. This reduced-order model which represents information for the dynamics of the wave groups is combined with a probabilistic analysis of the possible wave groups that can form stochastically for a given wave spectrum [10]. Note that stochasticity is inevitably introduced due to the 'mixing' between harmonics that propagate with different speeds due to dispersion. The resulted schemes provide a parsimonious and robust prediction scheme for unidirectional water waves.

The main purpose of the present paper is to extend the framework of Cousins and Sapsis [10] from their unidirectional context to multidirectional water waves. Several new challenges arise in this context that are absent in the unidirectional case. In the following section we review these challenges, summarize our framework and state the assumptions under which this reduced-order framework is applicable.

1.1. Summary of the framework

We seek to approximate the future spatiotemporal maximum wave height of a measured wave field by decomposing the field as the superposition of wave groups with simple shapes. The evolution of the simple wave groups are precomputed and stored, so that the prediction reduces essentially to an interpolation from an existing data set. This reduced-order approach can be divided into the following steps:

  I. Evolution of elementary wave groups.
 II. Decomposition of random wave fields.
III. Prediction of amplitude growth.

Step I. We consider spatially localized simple wave groups that can be expressed analytically and refer to them as *elementary wave groups* (EWG). In this paper we will use EWG with a Gaussian profile. One can alternatively use other shapes such as the secant hyperbolic used in [10]. The key requirement is that the EWG must be completely determined with only a few parameters. A Gaussian wave group, for instance, is determined by its amplitude (A_0), its longitudinal and transverse widths (L_x and L_y) and its orientation (θ) with respect to a global reference frame (see Fig. 1). Working with the Gaussian is also convenient since its derivatives with respect to parameters and variables take a simple form.

For a realistic range of these parameters, we evolve the corresponding elementary wave groups for T time units by numerically solving an appropriate wave envelope equation (see Section 2). We record the spatiotemporal maximum amplitude A_{max} that each EWG reaches over the time interval $[0, T]$. This step is computationally expensive but is carried out

only once. The resulting maximal amplitude is stored as a function of the parameters, i.e., $A_{max}(A_0, L_x, L_y, \theta)$. This step is carried out in Section 3.

Step II. Given a measured wave field, we approximate its envelope as a superposition of the elementary wave groups. To this end, the initially unknown positions, amplitudes and length scales of the elementary wave groups need to be determined such that their superposition provides a reasonable approximation of the measured wave field. In Section 4, we devise a dynamical systems-based method that determines the unknown parameters at a reasonable computational cost.

Step III. Once the measured wave field is decomposed into EWGs, its maximal future amplitude can be approximated by simply evaluating the precomputed function $A_{max}(A_0, L_x, L_y, \theta)$ for each set of EWG parameters (A_0, L_x, L_y, θ).

The above approach implicitly assumes that rogue waves form from individual wave groups through modulation instability [2]; a mechanism that has been observed in numerical simulations and in experiments [5,45]. It is known from linear random wave theory that rogue waves can also form due to the constructive interference of small-amplitude wave packets [26], especially for the case of short crested waves where modulation instability is not very pronounced. The probability of a rogue wave occurring through this linear mechanism, however, is orders of magnitude smaller than the ones generated through modulation instability [31,38,47]. We therefore neglect the rogue waves formed from superposition of smaller waves, and focus on the modulation instability of individual wave groups.

Also implicit in our approach is the assumption that the wave groups constructing a wave field have negligible interactions over the time interval $[0, T]$. This is of course not the case for large T. Cousins and Sapsis [10] find, however, that for intermediate time scales (10–40 wave periods) and for unidirectional waves this assumption is reasonable. We come to a similar conclusion for the two-dimensional surface waves considered here (see Section 5).

2. Envelope equation

To the first order, the modulations of a wave train with characteristic wave vector $\boldsymbol{k}_0$ and frequency $\omega_0 = \omega(\boldsymbol{k}_0)$ can be written as $\zeta(\boldsymbol{x}, t) = \frac{1}{2}u(\boldsymbol{x}, t) \exp[i(\boldsymbol{k}_0 \cdot \boldsymbol{x} - \omega_0 t)] + \text{c.c.}$, where u is the complex valued envelope for the modulation of the wave and c.c. is shorthand for complex conjugate terms. Assuming that the modulations are slowly varying (compared to the carrier wave), one can derive an equation for the envelope u of the free surface height ζ.

As shown by Trulsen et al. [43], for deep water, the most general form of the envelope equation can be written as

$$u_t + \frac{1}{4\pi^2} \int i(\omega(\boldsymbol{k} + \boldsymbol{k}_0) - \omega_0)e^{i\boldsymbol{k}\cdot(\boldsymbol{x}-\boldsymbol{\xi})}u(\boldsymbol{\xi}, t)\, \mathrm{d}\boldsymbol{\xi}\, \mathrm{d}\boldsymbol{k} + N(u) = 0, \tag{1}$$

where $N(u)$ denotes the nonlinear terms to be discussed shortly. The integral term is the exact form of the linear dispersion. The frequency $\omega(\boldsymbol{k} + \boldsymbol{k}_0)$ can be expanded in Taylor series around wavenumber $\boldsymbol{k}_0$. Truncating the series, and accordingly the nonlinear term $N(u)$, one obtains various approximate equations for the envelope u.

For instance, truncating the series at the second order and keeping the simplest cubic nonlinearity, one obtains the nonlinear Schrödinger (NLS) equation [48]. The NLS equation is only valid for wave spectra with a narrow bandwidth. To relax this limitation, Dysthe [15] derived the modified nonlinear Schrödinger (MNLS) equation by including higher-order terms in the truncation of (1). Rotating the spatial coordinate system $\boldsymbol{x} = (x, y)$ such that $\boldsymbol{k}_0 = (k_0, 0)^\top$, and normalizing the space and time variables as $t \mapsto \omega_0 t$ and $\boldsymbol{x} \mapsto k_0 \boldsymbol{x}$, the MNLS equation reads

$$u_t + \frac{1}{2}u_x + \frac{i}{8}u_{xx} - \frac{i}{4}u_{yy} - \frac{1}{16}u_{xxx} + \frac{3}{8}u_{xyy}$$
$$+ \frac{i}{2}|u|^2 u + \frac{3}{2}|u|^2 u_x + \frac{1}{4}u^2 u_x^* + iu\overline{\phi}_x|_{z=0} = 0, \tag{2}$$

where the last term involving the velocity potential is defined, using the Fourier transform $\mathcal{F}$, as

$$\overline{\phi}_x|_{z=0} = -\frac{1}{2}\mathcal{F}^{-1}\left[\frac{k_x^2}{|\boldsymbol{k}|}\mathcal{F}(|u|^2)\right],$$

with $\boldsymbol{k} = (k_x, k_y)$ being the wave vector.

The narrow bandwidth constraint can be further improved by including even more linear and nonlinear terms from equation (1) to obtain the broad-band MNLS (BMNLS) equation [42]. For the time scales considered here, however, the MNLS equation (2) provides an adequate model of gravity waves in deep ocean [44,46].

We numerically integrate the MNLS equation (2) on a finite two-dimensional domain $(x, y) \in [0, \ell_x] \times [0, \ell_y]$ with periodic boundary conditions (see Fig. 2). We set the domain size $2\ell_x = \ell_y = 200\pi$ (100 characteristic wavelength). As is discussed in Section 3, wave groups which are elongated transverse to the propagation direction have a better chance to give rise to rogue waves. The rectangular computational domain with a larger transverse dimension ($\ell_y = 2\ell_x$) is considered here in order to allow for several of these wave packets to fit in the domain.

The right-hand side of the MNLS equation is evaluated using a standard pseudo-spectral method, where the derivatives are computed in the Fourier domain and the nonlinear terms are computed in the physical domain. The temporal integration of the equations are carried out by a fourth-order Runge–Kutta exponential time differencing (ETD4RK) scheme [11]. This
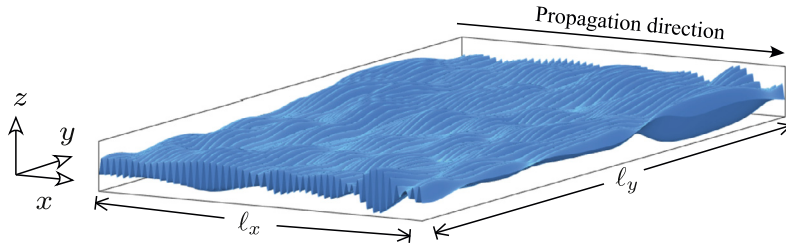
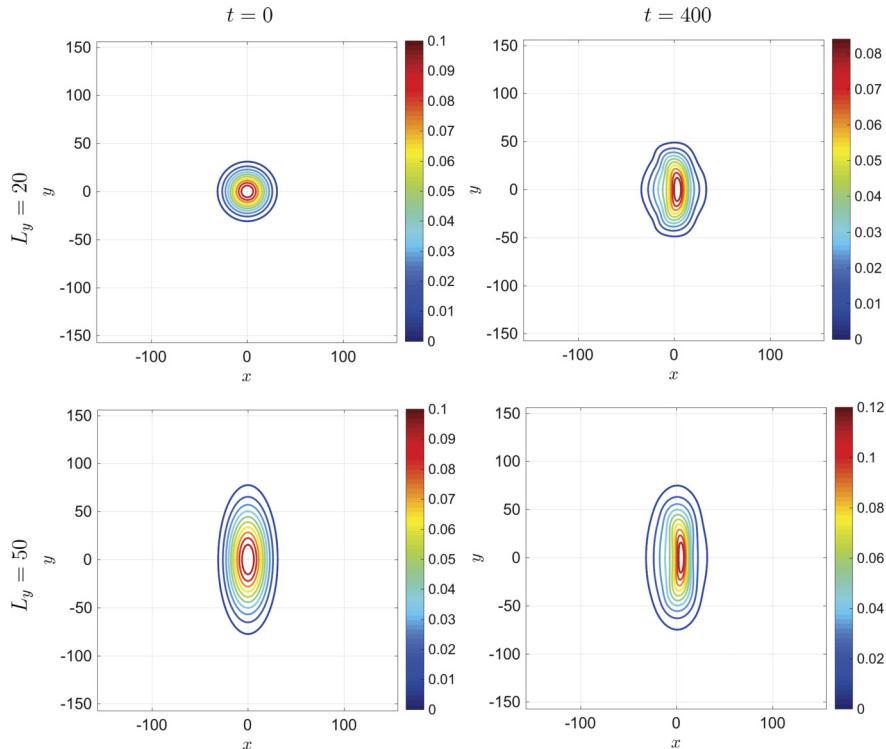**Fig. 2.** Schematic view of the computational domain.

Fig. 3. Initial Gaussian wave group with $L_x = 20$, $L_y = 20$ and $A_0 = 0.1$ (top row) and with $L_x = 20$, $L_y = 50$ and $A_0 = 0.1$ (bottom row). The color marks the wave height. (For interpretation of the references to color in this figure, the reader is referred to the web version of this article.)

method treats the linear part of the MNLS equation exactly, and uses the Runge–Kutta scheme for the evolution of the nonlinear terms. In the following computations, we use $2^9 \times 2^8$ Fourier modes to approximate the envelope $u(\boldsymbol{x}, t)$. The time-step size for the ETD4RK scheme is $\Delta t = 0.025$.

3. Evolution of elementary wave groups

We consider elementary wave groups with the Gaussian profile

$$u_0(x, y) = A_0 \exp\left[-\frac{x^2}{L_x^2} - \frac{y^2}{L_y^2}\right],\tag{3}$$

where the parameters L_x (controlling the width of the group in the longitudinal direction x), L_y (controlling the width of the group in the transverse direction y) and A_0 (controlling the amplitude of the group) determine the group completely. Note that, for simplicity, we set the orientation angle of the group θ to zero (see Fig. 1). This is motivated by the fact that wave groups tend to align with the propagation direction of the underlying wave train.

Using the MNLS equation, we evolve the initially Gaussian elementary wave groups (3) for a wide range of parameters (L_x, L_y, A_0). Fig. 3 shows two examples of the EWGs with the transverse widths $L_y = 20$ and $L_y = 50$. Both groups have the same longitudinal width $L_x = 20$ and amplitude $A_0 = 0.1$. Over time, the amplitude of the wave group with $L_y = 20$ decays monotonically and its lateral width grows slightly. The broader wave group with $L_y = 50$, however, undergoes focusing,
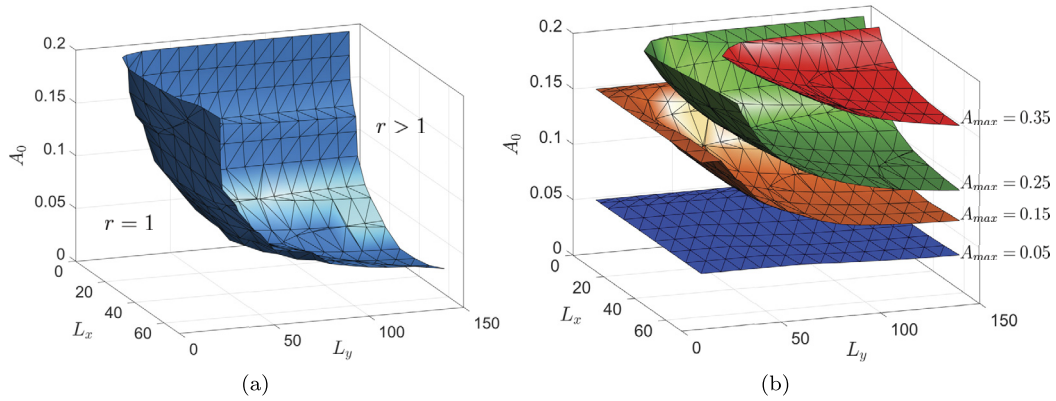
Fig. 4. (a) The hypersurface dividing the region between no amplitude growth ($r = 1$) from the region with amplitude growth ($r > 1$), where r is the amplitude ratio $r = A_{max}/A_0$. (b) Iso-surfaces of $A_{max} = \max_{x,y,t} |u(x, y, t)|$ corresponding to $A_{max} = 0.05$ (blue), $A_{max} = 0.15$ (orange), $A_{max} = 0.25$ (green) and $A_{max} = 0.35$ (red). (For interpretation of the references to color in this figure, the reader is referred to the web version of this article.)

whereby its amplitude increases and its longitudinal width decreases slightly. At later times $t > 450$, the amplitude of this wave group decays eventually.

If instead of the initial amplitude $A_0 = 0.1$, we choose a smaller amplitude (say $A_0 = 0.05$), the Gaussian EWG with $L_x = 20$ and $L_y = 50$ would not undergo amplitude growth either. These observations indicate that the focusing (or defocussing) of Gaussian EWGs depends nontrivially on all three parameters (L_x, L_y, A_0). Cousins and Sapsis [10] observe the same phenomena in the case of unidirectional waves, although in that case the parameter L_y is absent.

In order to analyze this parametric dependence systematically, we evolve the wave groups (3) for a range of parameters (L_x, L_y, A_0). The integration time here is $T = 1500$ (approximately 240 wave periods). For each parameter set, we record the maximum wave amplitude attained by the wave group,

$$A_{max} := \max_{x,y,t} |u(x, y, t)|, \tag{4}$$

where the maximum is taken over $x \in [0, \ell_x]$, $y \in [0, \ell_y]$ and $t \in [0, T]$. Note that the maximal amplitude A_{max} is a function of the parameters (L_x, L_y, A_0). We also define the amplitude ratio $r = A_{max}/A_0$ between the maximal amplitude A_{max} and the initial amplitude A_0. It is clear from definition (4) that $r \geq 1$. The values $r > 1$ indicate a focusing wave group, that is the amplitude of the EWG has increased over the time interval $[0, T]$.

Fig. 4(a) shows the hypersurface that forms the boundary between $r = 1$ and $r > 1$ as a function of the parameters (L_x, L_y, A_0). The elementary wave groups corresponding to the points below this surface do not undergo amplitude growth, while the points above the surface do. In other words, the displayed hypersurface forms the instability boundary for the EWGs in the parameter space (L_x, L_y, A_0).

Fig. 4(a) shows that the amplitudes of the EWGs with very small width in x or in y do not increase. More precisely, if $L_x < 2$ or $L_y < 10$, the EWG's amplitude decays, irrespective of the initial amplitude A_0. As it has been shown for unidirectional waves [9], this is a direct consequence of the scale-invariance breaking due to the additional terms of MNLS (compared with NLS). Here we observe the corresponding result for two-dimensional waves. For larger values of L_x and L_y, the amplitude growth (or lack thereof) depends on the initial amplitude. If the initial amplitude is too small (i.e., $A_0 \leq 0.05$), the wave amplitude will not grow at later times, irrespective of L_x and L_y. But if the initial amplitude exceeds a threshold (depending on L_x and L_y) we observe an amplitude growth.

This is further demonstrated in Fig. 4(b), showing a few iso-surfaces of the maximum amplitude A_{max} as a function of the parameters (L_x, L_y, A_0). We observe that the iso-surface $A_{max} = 0.05$ coincides with the surface $A_0 = 0.05$. This indicates that, regardless of the initial withs L_x and L_y, the amplitudes of the EWGs decay if the initial amplitude is small enough.

Iso-surfaces corresponding to larger values of A_{max} exhibit curved manifolds that correspond to the required combination of parameters (L_x, L_y, A_0) for the Gaussian EWG to reach the amplitude A_{max} at some time in the interval $[0, T]$.

For a finite L_x as the width L_y tends to infinity, we approach the unidirectional waves. Fig. 5 shows the instability boundary as one approaches this unidirectional limit. The solid curve (red color) corresponding to $L_y = 120$ is in agreement with available unidirectional results (cf. Fig. 2(b) from [10] and Fig. 3 of [9]).

In Section 5, we use the computed maximal amplitude $A_{max}(L_x, L_y, A_0)$ to estimate the amplitude growth of a given random wave field. To this end, we first need to approximate the random wave fields as a superposition of Gaussian EWGs (see section 4 below).

We point out that one can further generalize the choice of the EWG (3) by introducing a phase parameter, e.g. $u_0(x, y) = A_0 \exp[-x^2/L_x^2 - y^2/L_y^2] \exp[i\pi k_p x]$ where $k_p \ll k_0$ determines the phase of the modulating wave envelope. The elementary wave group (3) corresponds to $k_p = 0$ which simplifies the decomposition of the random wave fields into EWGs by reducing the number of free parameters. The effect of this choice ($k_p = 0$) on the resulting maximal amplitude A_{max} is insignificant (see Fig. 6(a)). However, the time when this amplitude is reached depends significantly on the phase (see Fig. 6(b)). As a
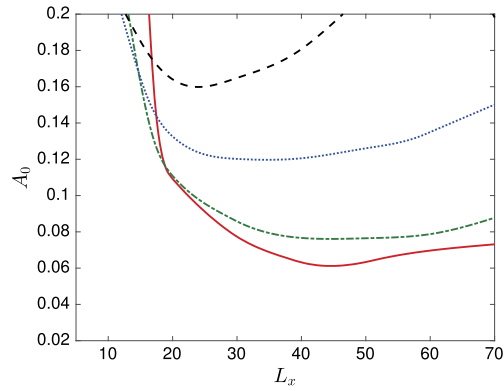
Fig. 5. The instability boundaries of Gaussian wave groups for various L_y. Each curve corresponds to a $L_y = $ constant slice of Fig. 4(a). Below each curve we have $r = 1$ (no focusing) while above the curve we have $r > 1$ (focusing). The curves correspond to $L_y = 15$ (dashed, black), $L_y = 30$ (dotted, blue), $L_y = 60$ (dash-dotted, green) and $L_y = 120$ (solid, red). (For interpretation of the references to color in this figure, the reader is referred to the web version of this article.)
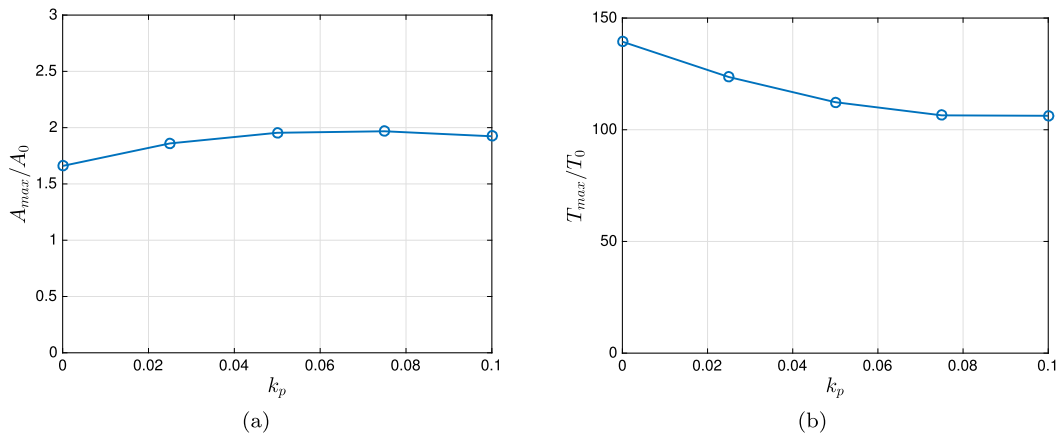

Fig. 6. The evolution of phase-dependent EWG $u_0(x, y) = A_0 \exp(-x^2/L_x^2) \exp(-y^2/L_y^2) \exp(i\pi k_p x)$ with $A_0 = 0.09$, $L_x = 30$, $L_y = 75$ and $0 \leq k_p \leq 0.1$. (a) The maximum amplitude A_{max} over the time interval $[0, T]$ with $T = 1500$. (b) The time T_{max} when the maximum amplitude A_{max} is reached. Here, $T_0 = 2\pi$ is the wave period.

result, our reduced-order prediction, which ignores the phase dependence, predicts the occurrence of a rogue wave over the future time window $[0, T]$ but not the exact time of its occurrence.

4. Decomposition of random wave fields

To apply the results of the wave group evolution we need to design a robust algorithm for the decomposition of any arbitrary wave field. Given such measured wave field, we approximate its envelope $|u_0|$ as a superposition of N Gaussian functions,

$$G(x, y) = \sum_{n=1}^{N} g_n(x, y), \tag{5}$$

where g_n is the n-th Gaussian elementary wave group,

$$g_n(x, y) = a_n \exp\left[-\frac{(x - x_n^c)^2}{(L_n^x)^2}\right] \exp\left[-\frac{(y - y_n^c)^2}{(L_n^y)^2}\right]. \tag{6}$$

The functions g_n are identical to the Gaussian EWGs (3), modulo a shift in the location of their peaks (x_n^c, y_n^c). The unknown parameters to be determined are

$$\boldsymbol{a} = (a_1, \cdots, a_N),$$
$$\boldsymbol{x}^c = (x_1^c, \cdots, x_N^c), \quad \boldsymbol{y}^c = (y_1^c, \cdots, y_N^c),$$

$$\boldsymbol{L}^x = (L_1^x, \cdots, L_N^x), \quad \boldsymbol{L}^y = (L_1^y, \cdots, L_N^y).$$

We first determine the location (x_n^c, y_n^c) of each Gaussian group from the local maxima of the envelope $|u_0|$. The local maxima can be readily located by a peak detection algorithm as detailed in Section 4.1. The corresponding amplitude a_n of each Gaussian wave group is determined by the amplitude of the envelope at the point (x_n^c, y_n^c), i.e., $a_n = |u_0(x_n^c, y_n^c)|$.

Once the centers $(\boldsymbol{x}^c, \boldsymbol{y}^c)$, and hence the amplitudes $\boldsymbol{a}$, are found, it remains to determine the width parameters $(\boldsymbol{L}^x, \boldsymbol{L}^y)$ of the Gaussian profiles. To this end, we use the following optimization step. Given the envelope $|u_0|$, we define the function

$$J(\boldsymbol{L}^x, \boldsymbol{L}^y) := \frac{1}{2} \int_0^{\ell_y} \int_0^{\ell_x} \left(G(x, y) - |u_0(x, y)| \right)^2 \mathrm{d}x\mathrm{d}y, \tag{7}$$

where G is the superposition of Gaussian wave groups (5) to be determined. The global minimizer of the function $J : \mathbb{R}^N \times \mathbb{R}^N \to \mathbb{R}$ returns the best Gaussian approximation to the envelope $|u_0|$.

Minimizing the functional J is a standard optimization problem. Here, we evaluate the minimizers by devising an appropriate fictitious-time differential equation as described in Section 4.2. This differential equation is the continuous limit of the gradient descent method and its trajectories are guaranteed to converge to stationary points of the functional J (see, e.g., section 6-6b of [33] or [17]). Before discussing the optimization method, however, we need to locate the peaks (x_n^c, y_n^c).

4.1. Detection of the peaks

There are several methods for detection of local maxima of a two-dimensional surface [34]. Here, we approximate the local maxima of the envelope $|u_0|$ by simply comparing the nearest neighbors on the given computational grid. On a rectangular grid, we declare a grid point a local maximum if the value of the envelope is larger than its eight immediate neighbors. For our purposes this rudimentary method returns satisfactory results and avoids the computational cost of more high-end peak detection algorithms.

Before applying this peak detection algorithm, however, we apply a low-pass filter to the measured envelope $|u_0|$. This filter is not an ad hoc smoothing; it is rather motivated by the observations made in Section 3. Recall that wave groups with lengths scales $L_x < 2$ or $L_y < 10$ decay regardless of their initial amplitude A_0. Since our purpose is to predict the growth of wave groups, we can safely neglect such small scale wave groups. Given this observation, therefore, we discard harmonics whose wavenumbers (k_x, k_y) satisfy

$$\frac{1}{2} \frac{\ell_x}{2\pi} < k_x \quad \text{or} \quad \frac{1}{10} \frac{\ell_y}{2\pi} < k_y. \tag{8}$$

Note that, given the domain size $\ell_x \times \ell_y$, these wavenumbers correspond to decaying wave groups with $L_x < 2$ or $L_y < 10$.

This physically-motivated smoothing has two advantages. First, it speeds up the computations by removing many irrelevant, small-scale peaks from the envelope. Second, as we further discuss in Section 4.3, it makes our group detection method robust to measurement noise.

4.2. Detection of the length scales

Once the peaks are detected, it remains to find the optimal set of length scales $(\boldsymbol{L}^x, \boldsymbol{L}^y)$ that minimizes the function $J : \mathbb{R}^N \times \mathbb{R}^N \to \mathbb{R}$ defined in (7). Here, we devise a dynamical systems-based method that can efficiently find these minimizers. The idea is to evolve $\boldsymbol{L}^x(\tau)$ and $\boldsymbol{L}^y(\tau)$ along the fictitious time τ such that the functional $J(\boldsymbol{L}^x(\tau), \boldsymbol{L}^y(\tau))$ decreases monotonically as τ increases. Differentiating with respect to the fictitious time τ, we obtain

$$\frac{\mathrm{d}J}{\mathrm{d}\tau} = \sum_{m=1}^N \iint \left(G(x, y) - |u_0(x, y)| \right) \left(\frac{\partial G}{\partial L_m^x} \frac{\mathrm{d}L_m^x}{\mathrm{d}\tau} + \frac{\partial G}{\partial L_m^y} \frac{\mathrm{d}L_m^y}{\mathrm{d}\tau} \right) \mathrm{d}x\mathrm{d}y, \tag{9}$$

where

$$\frac{\partial G}{\partial L_m^x} = 2a_m \frac{(x - x_m^c)^2}{(L_m^x)^3} e^{-(x-x_m^c)^2/(L_m^x)^2} e^{-(y-y_m^c)^2/(L_m^y)^2}, \tag{10a}$$

$$\frac{\partial G}{\partial L_m^y} = 2a_m \frac{(y - y_m^c)^2}{(L_m^y)^3} e^{-(x-x_m^c)^2/(L_m^x)^2} e^{-(y-y_m^c)^2/(L_m^y)^2}. \tag{10b}$$

We choose the fictitious-time derivatives $\mathrm{d}L_m^x/\mathrm{d}\tau$ and $\mathrm{d}L_m^y/\mathrm{d}\tau$ such that $J(\tau) := J(\boldsymbol{L}^x(\tau), \boldsymbol{L}^y(\tau))$ is monotonically decreasing. A trivial choice achieving this goal is
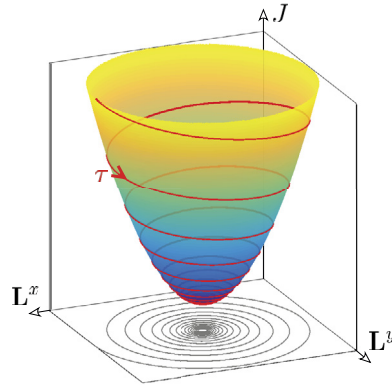
Fig. 7. Schematic geometry of the function (7) (color surface) and a trajectory of the ODE (11a), (11b) (red curve). Note that $\boldsymbol{L}^x, \boldsymbol{L}^y \in \mathbb{R}^N$ and that $J : \mathbb{R}^{2N} \to \mathbb{R}$ is a multivariable function. (For interpretation of the references to color in this figure, the reader is referred to the web version of this article.)

$$\frac{\mathrm{d}L_m^x}{\mathrm{d}\tau} = -\iint \left(G(x, y) - |u_0(x, y)| \right) \frac{\partial G}{\partial L_m^x} \mathrm{d}x \mathrm{d}y, \tag{11a}$$

$$\frac{\mathrm{d}L_m^y}{\mathrm{d}\tau} = -\iint \left(G(x, y) - |u_0(x, y)| \right) \frac{\partial G}{\partial L_m^y} \mathrm{d}x \mathrm{d}y, \tag{11b}$$

for $m = 1, 2, \cdots, N$.

The schematic Fig. 7 shows the geometry of the function J and a trajectory of the ODE (11a), (11b). In reality, the graph of J is much more complex with several local minima as opposed to one global minimum depicted here. If the ODE is solved from an initial condition $(\boldsymbol{L}_x(0), \boldsymbol{L}_y(0))$ far from the global minimum, the trajectory will most likely converge to a local minimum of the function J which could potentially result in an unsatisfactory approximation of the wave envelope. Therefore, it is important that the initial conditions $(\boldsymbol{L}_x(0), \boldsymbol{L}_y(0))$ are chosen carefully. Here, we choose these initial conditions such that the second-order partial derivative of the Gaussian wave group $g_n(x, y)$ evaluated at the corresponding peak (x_n^c, y_n^c) coincides with the second-order partial derivative of the measured envelope $|u_0|$ at that peak. More precisely, we choose $(L_n^x(0), L_n^y(0))$ such that

$$\partial_x^2 g_n(x_n^c, y_n^c) = \partial_x^2 |u_0|(x_n^c, y_n^c), \tag{12a}$$

$$\partial_y^2 g_n(x_n^c, y_n^c) = \partial_y^2 |u_0|(x_n^c, y_n^c). \tag{12b}$$

The derivatives of the measured envelope u_0 are approximated numerically by finite differences while the derivative of g_n are known analytically. Note that the value of the Gaussian g_n at the peak (x_n^c, y_n^c) is independent of the length scales (L_n^x, L_n^y). Similarly, the first-order partial derivatives of g_n vanish at the peaks and therefore are independent of the length scales (L_n^x, L_n^y). The lowest-order derivatives that depend on the length scales are the second-order derivatives. That is our motivation for using these derivatives to obtain good initial conditions $(L_n^x(0), L_n^y(0))$.

This choice of the initial conditions results in a reasonable approximation of the wave envelope $|u_0|$ such that all the envelopes reported in Section 5 below are reconstructed with relative error,

$$e_r = \frac{J}{\frac{1}{2} \iint |u_0(x, y)|^2 \mathrm{d}x \mathrm{d}y}, \tag{13}$$

smaller than 10%.

In order to evolve the ODE (11a), (11b), we use adaptive time stepping where the time step $\delta\tau$ is adjusted adaptively to ensure that the relative error e_r decreases after each time step. We elaborate this adaptive time stepping in Algorithm 1 where our wave group detection is summarized.

The accurate evaluation of the integrals in equation (11a), (11b) requires the wave envelope u_0 to be measured on a sufficiently dense spatial grid. The available wave gauges are capable of such high-resolution measurements [4,39]. However, if the wave measurements are only available on a sparse staggered grid, the parameters in the series (5) need to be estimated by an alternative method such as the statistical techniques of model inference (see Chapter 2 of [3] and Chapter 8 of [21] for a survey of these statistical methods). Here, we assume that a high-resolution measurement of the wave envelope is available so that the right-hand sides of differential equations (11a), (11b) can be evaluated accurately.

4.3. Sensitivity to measurement noise

In practice, the initial wave envelope u_0 is measured through a wave gauge with the ability to record the spatial surface elevation (see, e.g., [4,19,39]). Such measurements are inevitably contaminated with some degree of noise. It is therefore important to verify whether our wave group decomposition is robust with respect to such measurement noise.

Algorithm 1: Wave group detection algorithm. The variables $e_r^{(1)}$ and $e_r^{(2)}$ are relative errors which are evaluated according to equation (13). The inputs are the measured wave envelope $|u_0|$, an initial time step size $\delta\tau_0$, tolerance Tol and the maximum number of iterations MaxIter. ODEstep($\boldsymbol{L}^x(0), \boldsymbol{L}^y(0), \delta\tau$) denotes an explicit ODE time-stepping schema for (11a), (11b) with initial conditions ($\boldsymbol{L}^x(0), \boldsymbol{L}^y(0)$) and time step size $\delta\tau$. Here, the computations are carried out with $\delta\tau_0 = 2$, Tol $= 0.1$, MaxIter $= 10^5$ and the fourth-order Runge–Kutta for ODEstep.

Input: $|u_0|$, $\delta\tau_0$, Tol, MaxIter;
Detect peaks ($\boldsymbol{x}^c$, $\boldsymbol{y}^c$, $\boldsymbol{a}$) (see Section 4.1);
Determine ($\boldsymbol{L}^x(0), \boldsymbol{L}^y(0)$) according to (12a), (12b);
Evaluate $e_r^{(1)}$ with $J = J(\boldsymbol{L}^x(0), \boldsymbol{L}^y(0))$;
$i = 0$;
while $e_r^{(1)} > $ Tol *and* $i \leq$ MaxIter **do**
    $\delta\tau \longleftarrow \delta\tau_0$;
    $e_r^{(2)} \longleftarrow e_r^{(1)}$;
    while $e_r^{(2)} \geq e_r^{(1)}$ **do**
        $\delta\tau \longleftarrow \delta\tau/2$;
        $(\boldsymbol{L}^x, \boldsymbol{L}^y) \longleftarrow$ ODEstep($\boldsymbol{L}^x(0), \boldsymbol{L}^y(0), \delta\tau$);
        Evaluate $e_r^{(2)}$ with $J = J(\boldsymbol{L}^x, \boldsymbol{L}^y)$;
    end
    $(\boldsymbol{L}^x(0), \boldsymbol{L}^y(0)) \longleftarrow (\boldsymbol{L}^x, \boldsymbol{L}^y)$;
    $e_r^{(1)} \longleftarrow e_r^{(2)}$;
    $i \longleftarrow i + 1$;
end
Output: $\boldsymbol{x}^c$, $\boldsymbol{y}^c$, $\boldsymbol{a}$, $\boldsymbol{L}^x$, $\boldsymbol{L}^y$, $e_r^{(1)}$

To this end, we consider a noise-free envelope u_G consisting of the superposition of 50 Gaussian wave groups whose amplitudes, locations and length scales are chosen randomly. We add some artificial noise to this envelope to obtain the noisy envelope $u_0 = u_G + u_{noise}$. The noise u_{noise}, which is correlated in space, is obtained from a slowly decaying Gaussian spectrum with random phase. We use the ratio of the r.m.s. of $|u_{noise}|$ to the r.m.s. of $|u_G|$ as the noise to signal ratio to quantify the strength of the noise. Fig. 8(a) shows an example of such a wave filed with 10% noise. Panel (b) shows the wave field after applying the low pass filter discussed in Section 4.1 (cf. equation (8)). Panel (c) shows the reconstructed wave field from the Gaussian wave field approximation (5). The relative error e_r of this approximation is about 5.6%.

Fig. 8(d) shows the relative error e_r (see equation (13)) of the reconstructed wave fields for several levels of signal to noise ratio. The reconstructed wave fields have relative errors lower than 8% which is quite satisfactory given the fact that the wave gauges measure the surface elevation within 10% error to begin with [39].

The robustness of our wave field decomposition can be attributed to two features of the method. Firstly, the low pass filter discussed in section 4.1 results in a relatively smooth surface by removing the small scale fluctuations in the wave field (see Fig. 8(b)). As observed in Section 3 (cf. Fig. 4), whether these small scale fluctuations are attributed to noise or are genuine features of the wave field, they will not develop into rogue waves and they will not influence larger wave groups on their future evolution. Therefore, in the context of rogue wave detection, this low pass filter is justified.

The second reason for the robustness of our method is the spatial average taken in the cost function (7). As a result, the right-hand side of the ODEs (11a), (11b) involves an integral over space with an exponential kernel. This averaging adds an extra level of smoothing to our method. As opposed to the low pass filter, this smoothing is not applied directly to the measured wave field u_0; it is instead embedded in the minimization method itself.

5. Results and discussion

In this section, we examine the forecast skill of our method. To this end, we generate a large number of random wave fields that follow prescribed spectra. Then we decompose each field into Gaussian elementary wave groups using the method developed in Section 4. The future maximal amplitude of the random wave field is then estimated by interpolating the precomputed data $A_{max}(L_x, L_y, A_0)$ from Section 3.

5.1. Wave spectra

For the wave field, we consider envelopes of the form

$$\widehat{u}_0(\boldsymbol{k}) = \frac{2\pi}{\sqrt{\ell_x \ell_y}} \psi(\boldsymbol{k}) \exp[i\phi(\boldsymbol{k})], \tag{14}$$

where $\widehat{u}_0(\boldsymbol{k})$ denotes the Fourier coefficient of the envelope corresponding to the wave vector $\boldsymbol{k} = (k_x, k_y) \in \mathbb{Z}^2$. The phase $\phi(\boldsymbol{k})$ is a random variable uniformly distributed over the interval $[0, 2\pi]$. The spectrum of the waves generated from (14) coincide with $|\psi(\boldsymbol{k})|^2$.
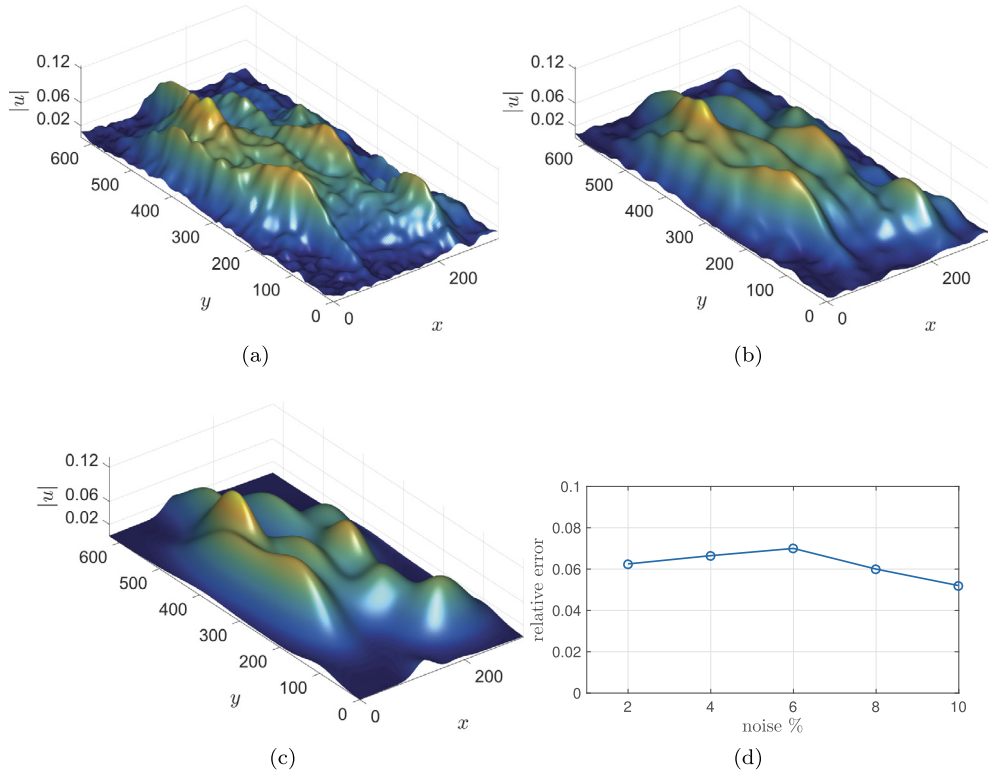
Fig. 8. (a) A wave field with 10% noise added to it. (b) The wave field after low-pass filtering. (c) Reconstructed wave group with Gaussian wave group approximation (5). (d) The relative error e_r of the reconstructed wave fields as a function of the noise to signal ratio.

Table 1

List of parameters for the five sets of simulations considered here. For the Gaussian spectra we have $\sigma_x = 0.035$ and $\sigma_y = 0.015$. For the JONSWAP spectra we set $\gamma = 3.3$, $\alpha = 0.04$. The remaining parameters are listed in the table.

	G1	G2	J1	J2	J3
Spectrum	Gaussian	Gaussian	Jonswap	Jonswap	Jonswap
Parameter	$\epsilon = 0.035$	$\epsilon = 0.053$	$\theta_0 = 40°$	$\theta_0 = 60°$	$\theta_0 = 80°$

We will consider two types of wave spectra: a Gaussian spectrum and the Joint North Sea Wave Observation Project (JONSWAP) spectrum. Following Dysthe et al. [16], the Gaussian spectrum is defined as

$$\psi(\mathbf{k}) = \frac{\epsilon}{\sqrt{2\pi\,\sigma_x\sigma_y}} \exp\left[-\frac{(q_x k_x)^2}{4\sigma_x^2} - \frac{(q_y k_y)^2}{4\sigma_y^2} \right], \tag{15}$$

where $q_x = 2\pi/\ell_x$ and $q_y = 2\pi/\ell_y$. For the JONSWAP spectrum we have

$$\psi(\mathbf{k}) = \frac{\alpha^{1/2}}{k^2} \exp\left[-\frac{5}{8}\left(\frac{k_0}{k}\right)^2 \right] \gamma^{r/2} \sqrt{D(\theta)}, \quad r = \exp\left[-\frac{(\sqrt{k} - \sqrt{k_0})^2}{2\sigma^2 k_0} \right]. \tag{16}$$

The directional spreading $D(\theta)$ is given by

$$D(\theta) = \begin{cases} \frac{2}{\theta_0} \cos^2\left(\frac{\pi\theta}{\theta_0}\right), & |\theta| \leq \frac{\theta_0}{2} \\ 0, & |\theta| > \frac{\theta_0}{2} \end{cases}, \tag{17}$$

where θ is the propagation direction and the parameter θ_0 is the directional spreading angle of the wave.

We consider five sets of experiments, two with the Gaussian spectrum and three with the JONSWAP spectrum as listed in Table 1. For the Gaussian spectrum we set $\sigma_x = 0.035$, $\sigma_y = 0.015$ and consider two sets of values for the remaining parameter, $\epsilon = 0.035$ (G1) and $\epsilon = 0.053$ (G2). The standard deviations σ_x and σ_y are chosen such that several wave groups fit in the computational domain. We choose $\sigma_y < \sigma_x$ since the waves tend to elongate orthogonal to the propagation direction of the wave train (the x-axis here). We also consider conservative values for the steepness ϵ to ensure the validity of the envelope equations (2).
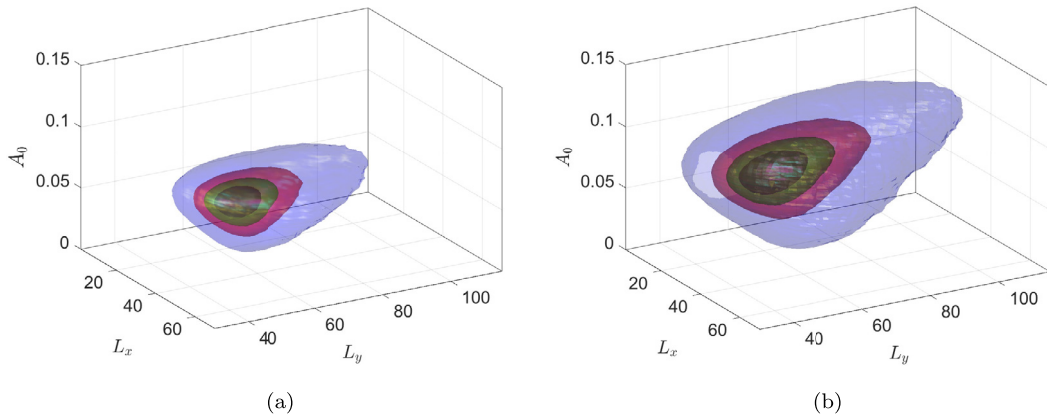
Fig. 9. Joint PDF of the detected Gaussian wave groups with length scales (L_x, L_y) and the wave amplitude A_0. Each PDF is extracted from $10,000$ realizations of random waves with Gaussian spectrum (15): (a) G1, (b) G2. The figures shows 5 isosurfaces of the PDFs, equispaced between 5% and 95% of the maximum PDF value.

Table 2
Statistics of the wave groups, rogue waves and their prediction. Here the wave period is $T_0 = 2\pi$ and the characteristic wave length is $\lambda_0 = 2\pi$.

	G1	G2	J1	J2	J3
$\langle A_0 \rangle$	0.050	0.075	0.054	0.053	0.052
$\langle L_x \rangle$	30.0	30.2	19.1	18.9	18.9
$\langle L_y \rangle$	67.7	68.2	53.8	36.4	28.3
A_0^c	0.087	0.087	0.092	0.097	–
L_x^c	32	31	20	21	–
L_y^c	76	76	63	47	–
rogue waves	11.7%	25.6%	2.2%	1.4%	0%
false negatives	4.9%	13.7%	1.4%	1.1%	–
false positives	3.9%	5.6%	0.2%	0.1%	0%
average warning time	$78T_0$	$40T_0$	$68T_0$	$72T_0$	–
average relative error	3.0%	9.2%	5.6%	5.0%	4.9%

For the JONSWAP spectrum, following Xiao et al. [47], we set $\sigma = 0.07$ for $k \leq k_0$ and $\sigma = 0.09$ for $k > k_0$. The peak enhancement factor is set to $\gamma = 3.3$ to conform to experimentally measured spectra [24]. The amplitude is set to $\alpha = 0.04$; this value is chosen so that the resulting average wave height is around 0.05, comparable to experiment G1. We investigate the effect of the spreading angle since this is the parameter that was absent in the unidirectional context considered previously by Cousins and Sapsis [10] and Farazmand and Sapsis [18]. As listed in Table 1, we consider two values of the spreading angle, $\theta_0 = 40°$ and $60°$ (experiments J1 and J2, respectively). For completeness we also consider a third spectrum with spreading angle $\theta_0 = 80°$ (experiment J3). In this latter case, however, we have no rogue waves occurring due to modulation instability, but nevertheless we will include J3 in our results to demonstrate the trends as the spreading angle increases.

5.2. Group detection and predictions

For each experiment G1-G2 and J1–J3, we generate $10,000$ wave fields (note that the phases ϕ in (14) are random). Using the group detection algorithm of Section 4, each wave field is decomposed into EWGs and the length scales L_x, L_y and amplitude A_0 of the wave groups are recorded.

The resulting parameters (L_x, L_y, A_0) span a wide range of values that depends on the shape of the spectrum. Fig. 9, for instance, shows the joint probability distribution function (PDF) of the wave group parameters (L_x, L_y, A_0) resulting from the simulations G1 and G2. As reported in Table 2, the average peak height of the detected wave groups for experiments G1 and G2 are $\langle A_0 \rangle = 0.05$ and $\langle A_0 \rangle = 0.075$, respectively. The larger average peak height in G2 (compared to G1) is expected as the parameter ϵ controls the average height of the resulting waves.

We observe that the mean length scales $\langle L_x \rangle$ and $\langle L_y \rangle$ are very similar for the two experiments G1 and G2 (see Table 2). This is also expected as the standard deviations σ_x and σ_y are identical for the two spectra. The standard deviation of the length scales L_x and L_y are significantly larger for the run G2 compared to G1. This is visibly appreciable from Fig. 9 that shows a broader joint PDF for the run G2, spanning a larger range of length scales, which is a direct consequence of the larger energy content of the spectrum in this case.

Next we examine the predictive power of the EWG decomposition. To this end, we generate $1,000$ random wave field envelopes u_0 for each parameter set G1 and G2. Each envelope is evolved, using the MNLS equation (2), for $T = 1500$ time
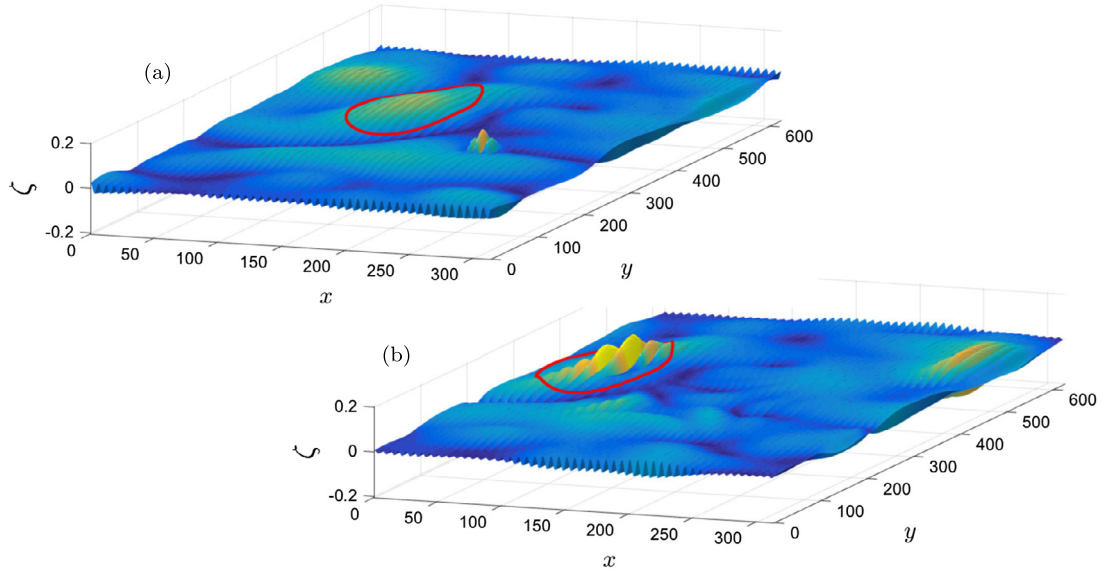
Fig. 10. A wave field generated from spectrum G2 at the initial time (a) and 175 wave periods later (b). The red curve marks the focusing wave group (identified at the initial time) that develops into a rogue wave. See the Supplementary Material for a movie.
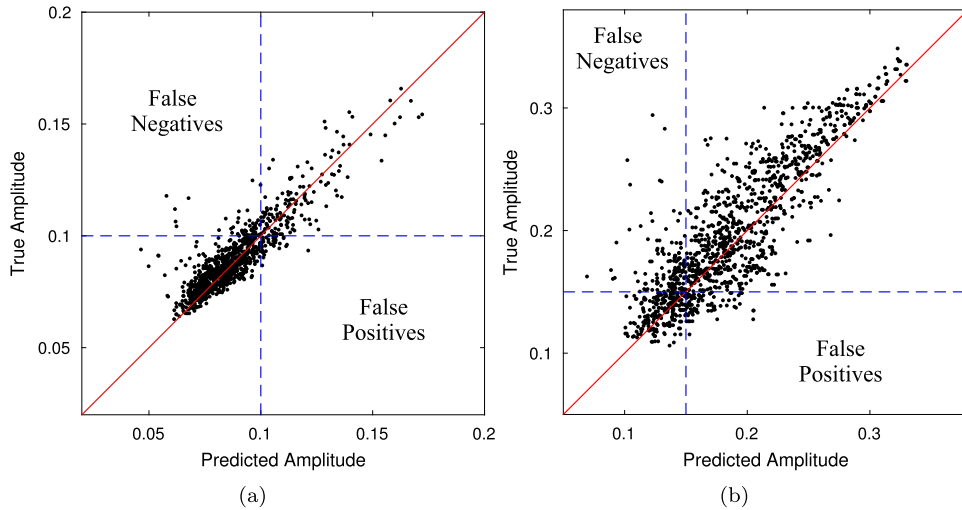

Fig. 11. Predicted maximal amplitude $\max_{x,y,t} |u(x,y,t)|$ from Gaussian group detection versus the true amplitude from direct numerical simulation of MNLS. (a) G1 (b) G2. The blue dashed lines indicate the magnitude of a rogue wave. (For interpretation of the references to color in this figure, the reader is referred to the web version of this article.)

units and the maximum spatiotemporal amplitude of the field $\max_{x,y,t} |u(x,y,t)|$ is recorded. We refer to $\max_{x,y,t} |u(x,y,t)|$ as the *true amplitude* of the wave.

We predict the maximal amplitude of each wave field by decomposing it into EWGs and interpolating the function A_{max} that is precomputed from Section 3. We refer to the maximal resulting amplitude as the *predicted amplitude* of the wave. An example of such prediction is shown in Fig. 10. The accuracy of the scheme is demonstrated in Fig. 11 that shows the true amplitudes versus the predicted amplitudes for the experiments G1 and G2. The figures for the JONSWAP experiments J1–J3 are similar (not presented here). As reported in Table 2, on average, the relative errors of the predictions are between 3% and 9.2%. The relative prediction error is defined here as the ratio of the difference between the true amplitude and the predicted amplitude divided by the true amplitude:

$$\text{relative prediction error} = \frac{\left|\text{true amplitude} - \text{predicted amplitude}\right|}{\text{true amplitude}}. \tag{18}$$

Given the approximations and assumptions underlying our reduced-order prediction, the resulting relative prediction errors of less than 9.2% are quite satisfactory.
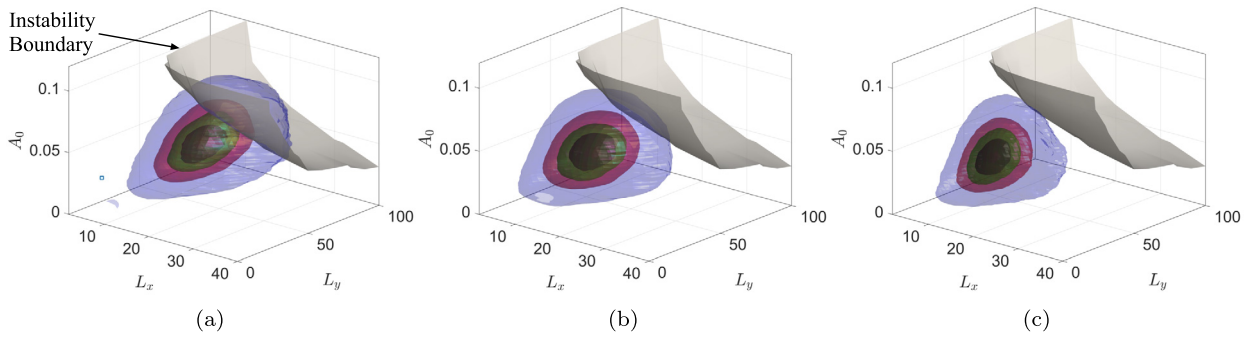
Fig. 12. Joint PDF of the detected Gaussian wave groups with length scales (L_x, L_y) and the wave amplitude A_0. Each PDF is extracted from 10,000 realizations of random waves with JONSWAP spectrum with the spreading angle $\theta_0 = 40°$ (a), $\theta_0 = 60°$ (b) and $\theta_0 = 80°$ (c). The figures shows 5 isosurfaces of the PDFs, equispaced between 5% and 95% of the maximum PDF value. The gray (dark) surface shows the instability boundary above which focusing instabilities form.
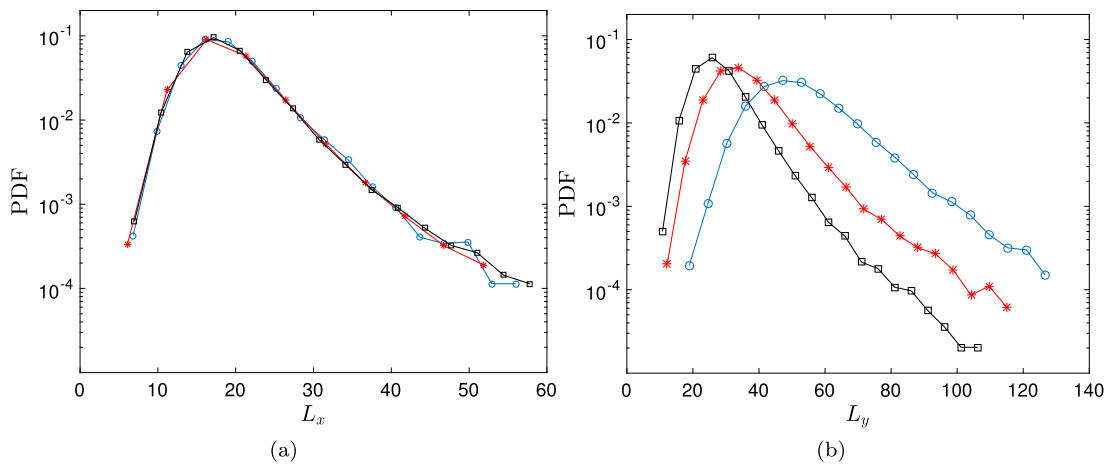

Fig. 13. PDF of the detected length scales L_x and L_y from JONSWAP simulations J1 (blue, circles), J2 (red, stars) and J3 (black, square). (For interpretation of the references to color in this figure, the reader is referred to the web version of this article.)

Now we consider the prediction of rogue waves using the reduced order method. Following the convention, we defined an extreme (or rogue) wave as one whose height $H = 2|u|$ exceeds twice the significant wave height H_s, where the significant wave height is defined as four times the standard deviation of the surface elevation: $H_s = 4\sqrt{\langle \zeta^2 \rangle}$. The dashed blue lines in Fig. 11 mark the resulting rogue waves threshold, i.e., $|u| = H_s$. First, we observe that, compared to G1, a higher percentage of wave field from experiment G2 produce rogue waves (see Table 2). This is to be expected as the spectral amplitude ϵ is larger in G2. As a result, the amplitude of individual wave groups tend to be larger for G2. Another contributing factor to this higher probability is the fact that the wave groups in G2 are more likely to have larger transverse length scales L_y (cf. Fig. 9).

We now turn to the experiments J1–J3 with the JONSWAP spectrum (16). Here, we focus on the directionality of the spectra controlled by the spreading angle θ_0, keeping all the other parameters fixed. Fig. 12 shows the PDF of the length scales of the detected EWGs obtained from 10,000 randomly generated wave fields. The average wave amplitudes $\langle A_0 \rangle$ and lengths scales $\langle L_x \rangle$ and $\langle L_y \rangle$ are reported in Table 2. We first observe that the average wave amplitudes $\langle A_0 \rangle \approx 0.05$ are similar for the three experiments J1–J3. In spite of this similarity, the frequency of rogue wave occurrence decreases as the spreading angle θ_0 increases. For the largest angle $\theta_0 = 80$, for instance, no rogue waves were produced from the 1000 wave fields considered. This is a well-known effect reported previously in several numerical and experimental studies (see, e.g., [30,47]).

The reason for this decreasing probability is clear from our wave group analysis presented in Fig. 12. As the spreading angle θ_0 increases the entire PDF shifts towards lower values of L_y, i.e. the average transversal length scale $\langle L_y \rangle$ decreases. This is better seen in the one-dimensional marginal PDFs shown in Fig. 13. Recall from Section 3 that the wave groups with smaller L_y require larger initial amplitude A_0 in order to focus (cf. Fig. 4). The wave fields with larger spreading angle tend to have wave groups with smaller transversal length scales L_y, while having similar wave amplitudes A_0. As a result, they are less likely to produce rogue waves. We point out that the distribution of the longitudinal length scales L_x are quite insensitive to the spreading angle θ_0 (see Fig. 13(a)).

We point out that the computational time required by the reduced-order prediction is significantly shorter than the time required for evolving the wave field under the envelope equation. For instance, evolving the wave fields under the MNLS equation for 100 wave periods (using the ETD4RK scheme with the time-step size $\Delta t = 0.025$ and $2^9 \times 2^8$ grid points) takes approximately 1800 seconds ($= 30$ minutes). Decomposing the same wave fields into the Gaussian EWGs, on the other hand, takes between 10 and 40 seconds. The variation in the decomposition time is due to the variations in the number of wave groups N (cf. Eq. (5)) that are present in different randomly generated wave fields.

5.3. Critical length scales and amplitudes

Recall from Section 3 that particular combinations of the length scales (L_x, L_y) and the amplitude A_0 are required for the wave group to evolve into a rogue wave. Then the natural question is: Given a particular wave spectrum, what critical combination (L_x, L_y, A_0) is most likely to produce rogue waves? The EWG evolution (Fig. 4) together with the PDFs of the detected groups (Figs. 9 and 12) are sufficient to answer this question.

For a given wave spectrum, let A_{ext} denote the amplitude threshold for a rogue wave. That is a wave with amplitude $|u| > A_{ext}$ constitutes a rogue wave. Following the conventional definition of a rogue wave (waves with height greater than twice the significant wave height H_s), we have $A_{ext} = H_s$. Considering the maximum amplitude function A_{max} shown in Fig. 4, the rogue waves lie above the critical surface

$$A_{max}(L_x, L_y, A_0) = A_{ext}. \tag{19}$$

Since this critical surface is a graph over (L_x, L_y) variables, the implicit function theorem [37] guarantees that there is a function $A_0^c : \mathbb{R} \times \mathbb{R} \to \mathbb{R}$ such that

$$A_{max}\big(L_x, L_y, A_0^c(L_x, L_y)\big) = A_{ext}, \tag{20}$$

for all L_x and L_y. The quantity $A_0^c(L_x, L_y)$ is the minimal initial amplitude required for an EWG with length scales (L_x, L_y) to develop into a rogue wave at some point in the future.

On the other hand, for a given wave spectrum, the probability distribution function $p(L_x, L_y, A_0)$ is computed in Section 5.2 (Figs. 9 and 12). Using this three-dimensional PDF, we define the conditional probability of a rogue wave with the given length scales L_x and L_y as

$$P_{ext}(L_x, L_y) = \int\limits_{A_0^c(L_x, L_y)}^{\infty} p(L_x, L_y, A_0)\mathrm{d}A_0, \tag{21}$$

where A_0^c is the critical amplitude defined in equation (20).

Fig. 14 shows the probability P_{ext} for the energy spectra listed in Table 1. Each probability function has a distinct peak at some length scales (L_x^c, L_y^c) reported in Table 2. We denote the associated critical amplitude $A_0^c(L_x^c, L_y^c)$ by A_0^c for simplicity. The physical interpretation of the triplet (L_x^c, L_y^c, A_0^c) is the following. For a given spectrum, rogue waves most likely develop from wave groups whose length scales are (L_x^c, L_y^c) and their amplitudes are larger than or equal to A_0^c. Roughly speaking, this means that the wave groups with length scales (L_x^c, L_y^c) and amplitudes larger than A_0^c are the 'most dangerous' both in terms of dynamics (i.e. they tend to evolve to rogue waves) and also in terms of probability of occurrence.

The critical values (L_x^c, L_y^c, A_0^c) are listed in Table 2 for each wave spectrum. Focusing on the spectra G1 and G2, we observe that the critical length scale $L_x^c \simeq 31$ is quite close to the average longitudinal lengths $\langle L_x \rangle \simeq 30$. In contrast, the critical length $L_y^c \simeq 76$ is significantly larger than the typical transverse length scale $\langle L_y \rangle \simeq 68$. The critical amplitude $A_0^c \simeq 0.087$ is also similar for the two spectra. The crucial difference is however the fact that the average amplitude of the wave groups for G2 ($\langle A_0 \rangle = 0.075$) is significantly larger than G1 ($\langle A_0 \rangle = 0.05$). As a result, the wave groups from G2 are more likely to achieve the critical amplitude for rogue wave formation. This explains the high rate of rogue wave formation (25.6%) observed for G2. Similar observations can be made about the spectra J1 and J2.

6. Summary and conclusion

Large waves form as a result of the dispersive mixing of smaller wave groups and the subsequent focusing due to nonlinear effects. Here we provide a method to quantify this mechanism in a reduced-order fashion. Specifically, we first develop a wave field decomposition algorithm that robustly and efficiently represents a wave field as a discrete set of elementary wave groups (EWGs) with Gaussian profiles. We then utilize the governing envelope equations to quantify the evolution of each of those elementary wave groups.

The combination of the wave field decomposition algorithm, which provides information about the statistics of the system (caused by the dispersive mixing of harmonics), and the precomputed map for the expected wave group elevation, which encodes dynamical information for focusing phenomena, allows for (i) the understanding of how the probability of occurrence of rogue waves changes as the spectrum parameters vary, (ii) the computation of a critical lengthscale characterizing wave groups with high probability of evolving to rogue waves, and (iii) the formulation of a robust and parsimonious reduced-order prediction scheme for large waves.
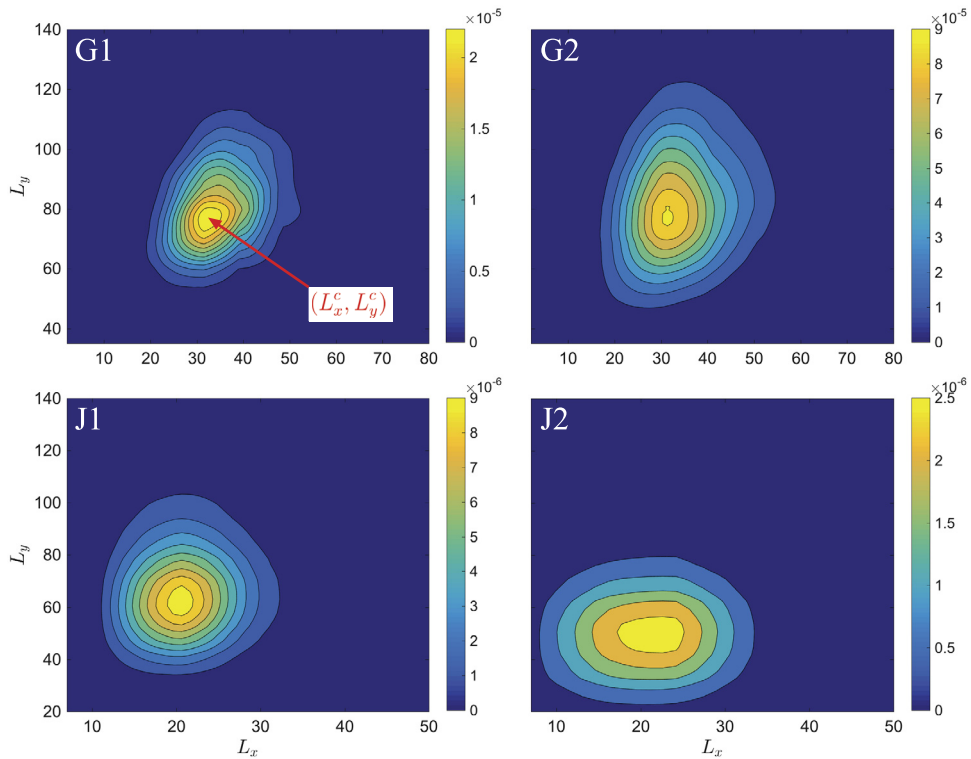
Fig. 14. The probability of rogue wave formation P_{ext} (21) as a function of the length scales L_x and L_y for the experiments G1–G2 and J1–J2. The probability for J3 is negligible and hence is not shown. The peak of P_{ext} marks the critical length scales (L_x^c, L_y^c).

Specifically, the EWG decomposition combined with the precomputed map provides information that complements the usual spectral analysis of the wave field, when it comes to large waves. For instance, it has been reported that the frequency of rogue wave occurrence is decreasing as the spreading angle increases. Our EWG analysis reveals that larger spreading angles lead to wave groups whose width in the transverse direction, L_y, tends to be smaller. This has a direct interpretation in terms of the probability of occurrence of rogue waves.

Through the same analysis we also identified a critical lengths scale for each direction (L_x^c, L_y^c) and a critical amplitude A_0^c associated with rogue waves. For each wave spectrum these are the most likely combination of scales and amplitudes that will eventually grow into a rogue wave. We found that the conditional probability of the critical length scales (L_x^c, L_y^c) is directly related to the frequency of rogue wave occurrence.

Regarding the prediction scheme, we showed, through extensive direct numerical simulations of the modified nonlinear Schrödinger (MNLS) equation, that the proposed reduced-order method is capable of predicting the future wave height with less than 10% relative error and a rogue-wave-prediction time window between 40 and 78 wave periods. The scheme is orders of magnitude less expensive compared with direct simulation methods and it is very robust with respect to measurement noise, which is inevitable in any realistic setting.

Our work can be extended in several directions. An important direction is the case of crossing seas where wave groups can carry more than one dominant wavenumber. Other scenarios where our analysis can be extended in a straightforward manner is the case of wave-current interaction and finite bathymetry. For such cases we expect that the stability and response surfaces will be modified in order to take into account the additional effect. In such cases, envelope equations may not be the best approach to characterize the dynamics of EWGs and more direct methods should be utilized. Clearly an important step forward is the experimental validation of the proposed scheme and we currently work towards this direction. The proposed approach provides an important paradigm of how the combination of dynamics and statistics can lead to better understanding of the system properties. In addition, it paves the way for the design of practical and robust prediction systems for large waves in the ocean.

Acknowledgements

Supplementary material

Supplementary content related to this article has been published online at 10.1016/j.jcp.2017.03.054.

References

[1] T.A.A. Adcock, R.H. Gibbs, P.H. Taylor, The nonlinear evolution and approximate scaling of directionally spread wave groups on deep water, Proc. R. Soc. A 468 (2145) (2012) 2704–2721.

[2] T.B. Benjamin, J.E. Feir, The disintegration of wave trains on deep water, part 1: theory, J. Fluid Mech. 27 (03) (1967) 417–430.

[3] C.M. Bishop, Neural Networks for Pattern Recognition, Oxford University Press, 1995.

[4] J.C.N. Borge, K. Reichert, K. Hessner, Detection of spatio-temporal wave grouping properties by using temporal sequences of X-band radar images of the sea surface, Ocean Model. 61 (2013) 21–37.

[5] A. Chabchoub, Tracking breather dynamics in irregular sea state conditions, Phys. Rev. Lett. 117 (2016) 144103.

[6] A. Chabchoub, N.P. Hoffmann, N. Akhmediev, Rogue wave observation in a water wave tank, Phys. Rev. Lett. 106 (20) (2011) 204502.

[7] G.F. Clauss, M. Klein, M. Dudek, M. Onorato, Application of higher order spectral method for deterministic wave forecast, in: Ocean Eng., vol. 8B, ASME, 2014, V08BT06A038.

[8] W. Cousins, T.P. Sapsis, Quantification and prediction of extreme events in a one-dimensional nonlinear dispersive wave model, Physica D 280 (2014) 48–58.

[9] W. Cousins, T.P. Sapsis, Unsteady evolution of localized unidirectional deep-water wave groups, Phys. Rev. E 91 (6) (2015) 063204.

[10] W. Cousins, T.P. Sapsis, Reduced-order precursors of rare events in unidirectional nonlinear water waves, J. Fluid Mech. 790 (2016) 368–388.

[11] S. Cox, P. Matthews, Exponential time differencing for stiff systems, J. Comput. Phys. 176 (2) (2002) 430–455.

[12] W. Craig, P. Guyenne, C. Sulem, Hamiltonian higher-order nonlinear Schrödinger equations for broader-banded waves on deep water, Eur. J. Mech. B, Fluids 32 (2012) 22–31.

[13] D.G. Dommermuth, D.K.P. Yue, A high-order spectral method for the study of nonlinear gravity waves, J. Fluid Mech. 184 (1987) 267–288.

[14] K. Dysthe, H.E. Krogstad, P. Müller, Oceanic rogue waves, Annu. Rev. Fluid Mech. 40 (2008) 287–310.

[15] K.B. Dysthe, Note on a modification to the nonlinear Schrödinger equation for application to deep water waves, Proc. R. Soc. A 369 (1736) (1979) 105–114.

[16] K.B. Dysthe, K. Trulsen, H.E. Krogstad, H. Socquet-Juglard, Evolution of a narrow-band spectrum of random surface gravity waves, J. Fluid Mech. 478 (2003) 1–10.

[17] M. Farazmand, An adjoint-based approach for finding invariant solutions of Navier–Stokes equations, J. Fluid Mech. 795 (2016) 278–312.

[18] M. Farazmand, T.P. Sapsis, Dynamical indicators for the prediction of bursting phenomena in high-dimensional systems, Phys. Rev. E 94 (2016) 032212.

[19] F. Fedele, A. Benetazzo, G.Z. Forristall, Space-time waves and spectra in the northern Adriatic sea via a wave acquisition stereo system, in: ASME 2011 30th International Conference on Ocean, Offshore and Arctic Engineering, 2011, pp. 651–663.

[20] G.Z. Forristall, Wave crest distributions: observations and second-order theory, J. Phys. Oceanogr. 30 (8) (2000) 1931–1943.

[21] J. Friedman, T. Hastie, R. Tibshirani, The Elements of Statistical Learning, Springer Series in Statistics, vol. 1, Springer, Berlin, 2001.

[22] T.C. Fu, A.M. Fullerton, E.E. Hackett, C. Merrill, Shipboard measurements of ocean waves, in: OMAE, 2011, pp. 1–8.

[23] O. Gramstad, K. Trulsen, Hamiltonian form of the modified nonlinear Schrödinger equation for gravity waves on arbitrary depth, J. Fluid Mech. 670 (2011) 404–426.

[24] K. Hasselmann, T. Barnett, E. Bouws, H. Carlson, D. Cartwright, K. Enke, J. Ewing, H. Gienapp, D. Hasselmann, P. Kruseman, et al., Measurements of Wind-Wave Growth and Swell Decay During the Joint North Sea Wave Project (Jonswap), Technical report, Deutches Hydrographisches Institut, 1973.

[25] P.A.E.M. Janssen, Nonlinear four-wave interactions and freak waves, J. Phys. Oceanogr. 33 (4) (2003) 863–884.

[26] M.S. Longuet-Higgins, On the statistical distribution of the heights of sea waves, J. Mar. Res. 11 (3) (1952) 245–266.

[27] C.C. Mei, M. Stiassnie, D.K.-P. Yue, in: Theory and Applications of Ocean Surface Waves: Nonlinear Aspects, vol. 23, 2005.

[28] J.C. Nieto Borge, K. Reichert, K. Hessner, Detection of spatio-temporal wave grouping properties by using temporal sequences of X-band radar images of the sea surface, Ocean Model. 61 (2013) 21–37.

[29] J.C. Nieto Borge, G.R. Rodríguez, K. Hessner, P.I. González, Inversion of marine radar images for surface wave analysis, J. Atmos. Ocean. Technol. 21 (8) (2004) 1291–1300.

[30] M. Onorato, A.R. Osborne, M. Serio, Extreme wave events in directional, random oceanic sea states, Phys. Fluids 14 (4) (2002) L25–L28.

[31] M. Onorato, A.R. Osborne, M. Serio, L. Cavaleri, C. Brandini, C.T. Stansberg, Observation of strongly non-Gaussian statistics for random sea surface gravity waves in wave flume experiments, Phys. Rev. E 70 (6) (2004) 067302.

[32] M. Onorato, S. Residori, U. Bortolozzo, A. Montina, F.T. Arecchi, Rogue waves and their generating mechanisms in different physical contexts, Phys. Rep. 528 (2) (2013) 47–89.

[33] D.A. Pierre, Optimization Theory with Applications, Dover Publishing, Inc., 1969.

[34] W.H. Press, S.A. Teukolsky, W.T. Vetterling, B.P. Flannery, Numerical Recipes: The Art of Scientific Computing, third edition, Cambridge University Press, 2007.

[35] V.P. Ruban, Anomalous wave as a result of the collision of two wave groups on the sea surface, JETP Lett. 102 (10) (2015) 650–654.

[36] V.P. Ruban, Gaussian variational ansatz in the problem of anomalous sea waves: comparison with direct numerical simulation, J. Exp. Theor. Phys. 120 (5) (2015) 925–932.

[37] W. Rudin, Principles of Mathematical Analysis, vol. 3, McGraw-Hill, New York, 1964.

[38] L. Shemer, A. Sergeeva, D. Liberzon, Effect of the initial spectrum on the spatial evolution of statistics of unidirectional nonlinear random waves, J. Geophys. Res., Oceans 115 (C12) (2010).

[39] W.R. Story, T.C. Fu, E.E. Hackett, Radar measurement of ocean waves, in: ASME 2011 30th International Conference on Ocean, Offshore and Arctic Engineering, 2011, pp. 707–717.

[40] M.A. Tayfun, Narrow-band nonlinear sea waves, J. Geophys. Res. 85 (C3) (1980) 1548–1552.

[41] S. Trillo, G. Deng, G. Biondini, M. Klein, G.F. Clauss, A. Chabchoub, M. Onorato, Experimental observation and theoretical description of multisoliton fission in shallow water, Phys. Rev. Lett. 117 (2016) 144102.

[42] K. Trulsen, K.B. Dysthe, A modified nonlinear Schrödinger equation for broader bandwidth gravity waves on deep water, Wave Motion 24 (3) (1996) 281–289.

[43] K. Trulsen, I. Kliakhandler, K.B. Dysthe, M.G. Velarde, On weakly nonlinear modulation of waves on deep water, Phys. Fluids 12 (10) (2000) 2432–2437.

[44] K. Trulsen, C.T. Stansberg, Spatial evolution of water surface waves: numerical simulation and experiment of bichromatic waves, in: The Eleventh International Offshore and Polar Engineering Conference, 2001.

[45] M.P. Tulin, T. Waseda, Laboratory observations of wave group evolution, including breaking effects, J. Fluid Mech. 378 (1999) 197–232.
[46] W. Xiao, Study of Directional Ocean Wavefield Evolution and Rogue Wave Occurrence Using Large-Scale Phase-Resolved Nonlinear Simulations, PhD thesis, Massachusetts Institute of Technology, 2013.
[47] W. Xiao, Y. Liu, G. Wu, D.K.P. Yue, Rogue wave occurrence and dynamics by direct simulations of nonlinear wave-field evolution, J. Fluid Mech. 720 (2013) 357–392.
[48] V.E. Zakharov, Stability of periodic waves of finite amplitude on the surface of a deep fluid, J. Appl. Mech. Tech. Phys. 9 (2) (1968) 190–194.